

1 **Soil and atmospheric drought explain the biophysical conductance responses in**
2 **diagnostic and prognostic evaporation models over two contrasting European forest**
3 **sites**

4 **K. Mallick^{1,2}, M. Sulis¹, T. Hu¹, and C.D. Jiménez-Rodríguez¹**

5 ¹Remote Sensing and Natural Resources Modeling, Department ERIN, Luxembourg Institute of
6 Science and Technology, Belvaux, Luxembourg.

7 ²Biometeorology Lab, Department of Environmental Science, Policy and Management,
8 University of California, Berkeley, California, United States.

9 Corresponding author: Kanishka Mallick (kaniska.mallick@gmail.com)

10 **Key Points:**

- 11 • Diagnostic (STIC1.2) and prognostic (CLM5.0) evaporation models show distinct levels
12 of sensitivity to water stress.
- 13 • STIC1.2 and CLM5.0 evaporation models better agree in simulating the energy fluxes as
14 compared to underlying biophysical conductance.
- 15 • Major differences in the simulated stomatal conductance are due to divergences in the
16 physiological assumptions of the two evaporation modelling approaches.
17

18 Abstract

19 Diagnosing and predicting evaporation through satellite-based surface energy balance (SEB) and
20 land surface models (LSMs) is challenging due to the non-linear responses of aerodynamic (g_a)
21 and stomatal conductance (g_{cs}) to the coalition of soil and atmospheric drought. Despite a soaring
22 popularity in refining g_{cs} formulation in the LSMs by introducing a link between soil-plant
23 hydraulics and g_{cs} , the utility of g_{cs} has been surprisingly overlooked in SEB models due to the
24 overriding emphasis on eliminating g_a uncertainties and the lack of coordination between these
25 two different modeling communities. Therefore, a persistent challenge is to understand the
26 reasons for divergent evaporation estimates from different models during strong soil-atmospheric
27 drought. Here we present a virtual reality experiment over two contrasting European forest sites
28 to understand the apparent sensitivity of the two critical conductances and evaporative fluxes to a
29 water-stress factor (β -factor) in conjunction with land surface temperature (soil drought proxy)
30 and vapor pressure deficit (atmospheric drought proxy) by using a non-parametric diagnostic
31 model (Surface Temperature Initiated Closure, STIC1.2) and a prognostic model (Community
32 Land Model, CLM5.0). Results revealed the β -factor and different functional forms of the two
33 conductances to be a significant predictor of divergent response of the conductances to soil and
34 atmospheric drought, which subsequently propagated in the evaporative flux estimates between
35 STIC1.2 and CLM5.0. This analysis reaffirms the need for consensus on theory and models that
36 capture the sensitivity of the biophysical conductances to the complex coalition of soil and
37 atmospheric drought for better evaporation prediction.

38 Plain Language Summary

39 Water lost by plants through evaporation is strongly regulated by two important physical and
40 biological attributes, namely aerodynamic and stomatal conductance. The magnitude and
41 variability of these conductances and their degree of regulation on evaporation is heavily
42 dependent on how the conductances respond to the conjugate dryness from the soil and the
43 atmosphere. Because these conductances cannot be typically measured at a large scale, the
44 majority of the global evaporation models use different mechanistic functions to estimate them,
45 which involves many empirical parameters. Such methods do not fully capture the evaporation
46 variability of ecosystems during water stress, leading to large errors in water cycle monitoring.
47 Our model-based synthetic experiment shows how two structurally different models with
48 different functional forms of the conductances respond very differently to emerging soil-
49 atmospheric water stress and produce divergent estimates of evaporation in a variety of dry and
50 wet conditions. While this study offers a greater insight into the role of conjugate effects of soil
51 and atmospheric drought in explaining the conductances and evaporation variability, it also
52 shows a novel perspective to reconcile predictive and remote sensing evaporation models for
53 water management applications, testing theory of plant water use and land-atmosphere
54 interactions.

55 **1 Introduction**

56 Soil and atmospheric droughts are triggered by enhanced land surface drying and climate
57 warming. As a result, they feedback to some of the fundamental drivers of terrestrial evaporation
58 namely, land surface temperature (LST) and atmospheric vapor pressure deficit (D_a), which
59 subsequently affects climate and physiology of terrestrial ecosystems (Morrow and Friedl, 1998;
60 Liao et al., 2020). While their coalition controls the magnitude and variability of the surface
61 energy balance (SEB) components (Thakur et al., 2021, Mallick et al., 2022), they are
62 simultaneously modulated by the SEB partitioning (Kustas and Anderson, 2009; Anderson et al.,
63 2012; Mallick et al., 2018, 2022). LST is very sensitive to soil water content variations and
64 captures additional information on the biophysical controls on surface temperature, such as
65 evaporative cooling and stomatal conductance variations (Kustas and Anderson, 2009; Anderson
66 et al., 2012; Mallick et al., 2016, 2022). While LST serves as a key diagnostic variable to
67 monitoring land surface biophysical states (Green et al., 2022), it is also a prognostic indicator of
68 their evolution under global warming and land use change (Chen and Dirmeyer, 2020). On the
69 other hand, D_a is expected to rise over ecosystems due to the combination of increased LST,
70 reduced soil water content, and decreased relative humidity due to low evaporation (Byrne &
71 O'Gorman, 2013). An elevated D_a increases the atmospheric demand for evaporation (Monteith,
72 1965; Penman, 1948), and it simultaneously reduces (enhances) stomatal (aerodynamic)
73 conductance (Damour et al., 2010; Medlyn et al., 2011; Mott, 2007). Therefore, understanding
74 the conductance response to these two opposing effects of changes in D_a due to surface
75 temperature warming is crucial for assessing the impacts of soil and atmospheric drought on
76 evaporation for better water cycle assessment through different models (Massman et al., 2019).

77 LST-based diagnostic monitoring and mapping of evaporation varies from multiple
78 spatio-temporal scales and involves a host of models (Bhattarai et al., 2018; 2019). The most
79 common approach (Anderson et al., 2007) centres on assuming a physical model of evaporation
80 in the framework of SEB and many of the variables required to compute evaporation using the
81 SEB models are available directly as satellite products (e.g., vegetation index, albedo, leaf area
82 index, vegetation cover). What is common to all the approaches is that they rely to a greater
83 extent on parameterization of physical surface characteristics and plant biological attributes for
84 deriving an estimate of evaporation. Two such important characteristics are the aerodynamic
85 conductance and canopy-surface conductance and thus the diagnostic estimates of evaporation
86 from the conventional approaches are conditional on their parameterizations (Kustas et al., 2016;
87 Trebs et al., 2021). The current bottlenecks are that LST-based diagnostic approaches involve
88 significant structural complexity with respect to parameterization of soil and aerodynamic
89 conductance, the lack of a physically-based aerodynamic conductance model (Holwerda et al.,
90 2012), and bypassing the role of LST versus stomatal conductance interactions in evaporation
91 (Mallick et al., 2022).

92 LSMs are useful tools for predicting long-term records of LST across a wide range of
93 spatial scales. These prognostic time series are iteratively computed by parameterizing the land
94 surface energy fluxes using Monin-Obukhov similarity theory (e.g., Sellers et al., 1986). These
95 time series have been exploited for investigating the role of LST in modulating the land surface
96 energy partitioning (Gao et al., 2004; Zeng et al., 2012) and exploring the relationship between
97 LST diurnal cycle and the degree of land-atmosphere coupling strength through multi-model
98 experiments (Koster et al., 2004, 2006). The LSM-simulated LST records have been also

99 blended with thermal infrared (TIR) remote sensing data using various postprocessing techniques
100 to obtain a complete spatiotemporal dataset that overcome the limitations of both prognostic and
101 diagnostic LST information (Siemann et al., 2016; Long et al., 2020; Zhang et al., 2021). On the
102 other hand, many previous validation and comparison studies based on the use of in-situ and
103 remote sensing data have shown persistent limitations of LSMs in realistically simulating this
104 essential climate variable of the Earth system (e.g., Mitchell et al., 2004; Zheng et al., 2012;
105 Wang et al., 2014; Trigo et al., 2015, Koch et al., 2016). These systematic evaluations have led
106 to continuous improvements in LSMs formulations related to the parameterized roughness length
107 for heat (Chen et al., 2010), soil thermal conductivity (Zeng et al., 2012), and soil evaporation
108 resistance (Ma et al., 2021). For instance, Yuan et al. (2021) used MODIS LST data product to
109 validate a revised surface roughness scheme of the Common Land Model (CoLM). Similarly,
110 Meier et al. (2022) verified a series of modifications of the surface roughness in the Community
111 Land Model (version 5.1) by assessing the improvements in the simulated LST diurnal cycle for
112 different land cover types. Despite the improved model performances and underpinning the
113 prominent role of LST in the predictive skills of LSMs, it remains difficult to fully disentangle
114 the processes and feedback mechanisms through which changes and biases in LST propagate
115 into the simulated vegetation biophysical interactions.

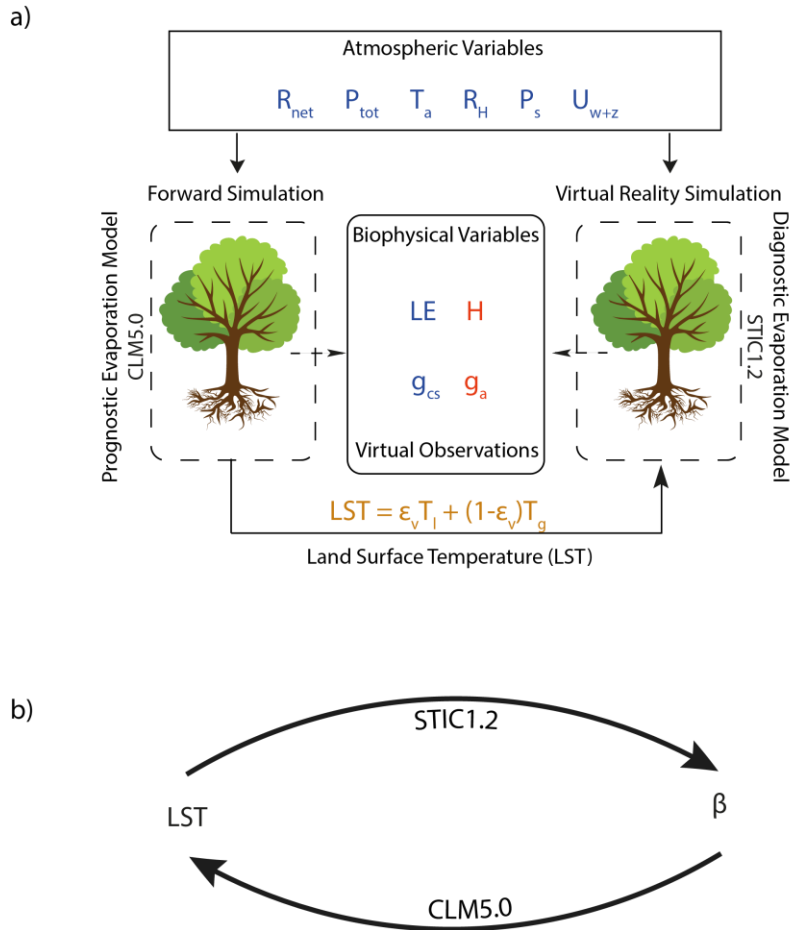
116 Several studies have exploited the synergies between remote sensing-based evaporation
117 models and Land Surface Models (LSMs) for acquiring a better understanding of land surface
118 energy partitioning, land-atmosphere interactions, and couplings of the water-carbon cycles
119 (Levine et al., 2016; Gevaert et al., 2017, among many others). These studies have employed
120 LSMs of varying complexity and remote sensing-based products relying on diverse sources of
121 information extracted from different spectral wavebands of satellite sensors. In this framework,
122 Long et al. (2014) assessed the evaporation estimates from four different LSMs and two remote
123 sensing products. They found that the uncertainty is lower in LSMs and that such uncertainty is
124 resolution-dependent, with lower uncertainty at coarser spatial resolutions. Similar findings were
125 reported by Wang et al. (2015) that compared the evaporation output from three different LSMs
126 with an evaporation product based on MODIS data over Canada. Zhang et al. (2020) proposed a
127 systematic evaluation and comparison of multiple evaporation data models over the contiguous
128 United States. This effort was carried out within the North American Land Data Assimilation
129 System (NLDAS) where multiple LSMs are integrated and compared against different remote
130 sensing-based evapotranspiration products (e.g., GLEAM and MODIS-based dataset). Results of
131 this study indicated a general agreement in the spatial patterns and seasonal evaporation of the
132 different data output, despite a broad range of estimates within both prognostic and diagnostic
133 class of models. Overall, these studies were critical to identifying strengths and weaknesses of
134 the various evaporation products, providing guidelines for models' improvements and effective
135 strategies to reduce uncertainties. However, none of these studies have compared the underlying
136 biophysical interactions and feedback mechanisms explaining the link between evaporation,
137 LST, and the associated conductances (i.e., aerodynamic, and stomatal) in diagnostic (i.e.,
138 remote sensing-based) and prognostic (i.e., LSMs) models. This is because most of the remote
139 sensing-based evaporation models use surface parameterizations (i.e., surface roughness,
140 atmospheric stability and conductances) that are very similar to those that are implemented in
141 LSMs and that show limited predictive capabilities and high uncertainties (El Ghawi et al.,
142 2023). This is an obvious limiting factor impeding an independent and stringent benchmarking of
143 the inherent assumptions of prognostic and diagnostic evaporation models.

144 To summarize, while LST is used as a critical boundary condition to understand drought-
145 induced variability in evaporation in the diagnostic models, D_a is used as an important boundary
146 condition to understand both LST and evaporation variability in the prognostic models. The
147 explanatory potential of evaporation variability in both the approaches depends on how well the
148 biophysical conductances in the models respond to the coalition of soil and atmospheric drought.
149 The present study introduces a virtual reality numerical framework where the non-parametric
150 remote sensing evaporation model STIC1.2 (Mallick et al., 2018, 2022) is driven using two
151 configurations: (i) LST signal simulated by the state-of-the-art LSM CLM5.0 (Lawrence et al.
152 2019); and (ii) LST retrieved from thermal infrared remote sensing data products. The latter are
153 also used to assess the predictive skills of CLM5.0 in reproducing the LST under different plant
154 water stress conditions. This numerical framework aims at comparing the role of LST magnitude
155 and variability on the biophysical conductances in STIC1.2 and CLM5.0 and assessing the
156 relative sensitivity of the biophysical conductances to LST and ancillary environmental variables
157 in diagnostic (STIC1.2) and prognostic (CLM5.0) evaporation modeling approaches. The virtual
158 reality framework is established at two forested sites in Europe, with contrasting environmental
159 conditions, different plant functional types, and spanning a temporal length characterized by
160 strong interannual climate variability.

161 **2 Methods and Data**

162 **2.1 Study sites**

163 This study considered two contrasting forested sites in Europe, namely Puéchabon
164 (43.74°N, 3.60 °E, France, FR-Pue) and Loobos (52.17°N, 5.74°E, Netherlands, NL-Loo). FR-
165 Pue site has a Mediterranean climate with a mean annual temperature of 13.8 °C and a mean
166 annual precipitation of 914 mm yr⁻¹. The site is characterized by dry and hot summers reaching a
167 maximum vapor pressure deficit of 6.0 kPa; Csa class according to the Köppen-Geiger
168 classification (Beck et al., 2018). The site has a shallow soil layer (< 1m depth) with a clay loam
169 texture (Reichstein et al., 2002) sitting on top of a hard limestone formation (Cabon et al., 2018).
170 The vegetation cover is classified as evergreen broadleaf due to the dominance of *Quercus ilex*
171 L. trees. NL-Loo site has a mean annual temperature of 10.0 °C and a mean annual precipitation
172 of 754 mm yr⁻¹. This temperate climate is characterized by warm summers without a dry season
173 and maximum vapor pressure deficit around 4.3 kPa; the site has an Oceanic climate (Cfb)
174 following the Köppen-Geiger classification. The site is sitting on top of ice-pushed deposits
175 giving origin to a sandy loam soil with more than 30 m of depth (Tiktak and Bouten, 1994). The
176 land cover is evergreen needleleaf with *Pinus sylvestris* L. as the dominant tree species. The
177 meteorological observations of these two sites were obtained from the FLUXNET2015 dataset
178 (Pastorello et al., 2020), spanning over the 2001-2014 and 2002-2013 periods for FR-Pue and
179 NL-Loo, respectively. These long-time records embed strong interannual variability including
180 severe droughts as the 2003 continental and the 2006/2010 regional heat wave and drought
181 events in Europe.



182

183 **Figure 1. (a)** Conceptual diagram of the virtual reality experiment. While the SEB fluxes and
 184 conductance outputs of forward simulation from CLM5.0 is used as virtual reality observation,
 185 LST output is further used to drive STIC1.2 simulation with the same environmental drivers. The
 186 fluxes and conductance outputs from STIC1.2 are subsequently analyzed with respect to the
 187 virtual reality. **(b)** Diagram illustrating the relationship between LST and simulated water stress
 188 factor in the diagnostic STIC1.2 and prognostic CLM5.0 approach.

189

2.2 Diagnostic and Prognostic Evaporation Models

190

2.2.1 Surface Temperature Initiated Closure – STIC1.2

191

192 STIC1.2 is a non-parametric evaporation model which perceives the vegetation-
 193 atmosphere system as a box and considers evaporation as both the driver and driven by different
 194 biophysical states in the vegetation-atmosphere system (Mallick et al., 2022). Assuming the
 195 surface-atmosphere exchange operates within the available environmental and water limits,
 196 STIC1.2 estimates evaporation by finding analytical solution of the biophysical conductances
 197 from the known boundary conditions of the box that is, solar radiation (R_g), air temperature (T_a),
 198 relative humidity (rH), and LST (Mallick et al., 2018, 2022; Trebs et al., 2021). The main
 199 biophysical states are the aerodynamic temperature, aerodynamic conductance, and canopy-
 200 surface conductance, respectively. Considering vegetation-soil-substrate as a single slab,
 201 STIC1.2 implicitly assumes the aerodynamic conductances from individual air-canopy and
 canopy-substrate components to be the ‘effective’ aerodynamic conductance for energy and

202 water vapor (i.e., g_a), and surface conductance from individual canopy (stomatal) and
203 soil/substrate complexes to be the ‘effective’ canopy-surface conductance (i.e., g_{cs}) which
204 simultaneously regulates the exchanges of sensible and latent heat fluxes between the surface
205 and the atmosphere.

206 The explicit assumptions of STIC1.2 include the (a) first order dependence of evaporative
207 fraction on water stress, g_a and g_{cs} ; (b) direct feedback between water stress with g_a , and g_{cs}
208 driven by LST sensitivity to water stress variations; and (c) STIC1.2 uses LST-air temperature
209 difference in the model as a proxy of soil-vegetation water stress and assume that the difference
210 between LST-air temperature can explain the soil moisture induced variability in conductances
211 and fluxes.

212 By integrating LST with surface energy balance (SEB) theory and vegetation biophysical
213 principles, STIC1.2 formulates multiple state equations to eliminate the need for any empirical
214 parameterizations of the conductances. The state equations are related to LST through an
215 aggregated water stress factor (I_{sm}) and the effects of LST are subsequently propagated into the
216 analytical solutions of the conductances through the water stress (Supporting Information, in
217 Mallick et al., 2022). The inputs needed for the computation of conductances and SEB fluxes in
218 STIC1.2 are T_a , LST, rH or air vapor pressure (e_a), and downwelling and reflected global
219 radiation (R_g and R_r).

220 2.2.2 Community Land Model version 5.0 – CLM5.0

221 CLM5.0 is a state-of-the-art LSM that simulates the land surface biogeophysical,
222 biogeochemical, and hydrological processes that control the exchange of water, energy, and
223 matter fluxes at the land-atmosphere interface. Here we provide a brief discussion of the key
224 elements of CLM5.0 that are investigated in the virtual reality numerical framework, whilst a
225 comprehensive description of the model structure can be found in Lawrence et al. (2019) and of
226 the model formulations in the user manual documentation (Lawrence et al., 2018). The land
227 surface energy fluxes, namely sensible and latent heat fluxes, are calculated using separated
228 vegetation and ground surfaces and discriminating between shaded and sunlit vegetation
229 components. The energy fluxes are calculated based on the Monin-Obukhov similarity theory
230 through an iterative procedure solving for vegetation and ground temperature. In this procedure,
231 the aerodynamic conductance, which expresses the efficiency of the turbulent transfer of heat,
232 momentum, and water vapor is calculated as a function of plant-specific parameters (i.e.,
233 displacement height, roughness length) and adjusted according to atmospheric stability
234 conditions. CLM5.0 uses the coupled stomatal conductance and photosynthesis model following
235 Medlyn et al. (2011), where the leaf water potential calculated by the plant hydraulic system
236 (Kennedy et al., 2019) serves as indicator for water stress conditions through an attenuation of
237 the maximum carboxylation (biochemical limitation). The calculated leaf water potential is also
238 used for the continuous update (in analogy to the soil characteristics curves) of plant hydraulic
239 properties through the definition of a plant vulnerability curve for each segment (i.e., roots,
240 xylem, and sunlit and shaded leaf segments) of the vegetated surface. For further details on the
241 calculation of the water stress factor (β -factor) in the plant hydraulic system of CLM5.0 the
242 reader is referred to Kennedy et al., (2019).

243 2.3 Virtual Reality Framework

244 The virtual reality framework is created by running the STIC1.2 model under two
 245 different configurations. In the first configuration (scenario-1), the LST simulated by CLM5.0 is
 246 used as virtual reality to drive the STIC1.2 model. The LST in CLM5.0 is computed based on the
 247 leaf temperature (T_{leaf}) and the temperature of the ground (T_{grnd}):

$$248 \quad LST = \varepsilon_v T_{leaf} + (1 - \varepsilon_v) T_{grnd}$$

249 where the vegetation emissivity ε_v is calculated as function of the LAI, SAI, and the average
 250 inverse optical depth for longwave radiation (set to 1 in CLM5.0). All the variables are computed
 251 at hourly time steps.

252 In the second configuration (scenario-2), STIC1.2 is run in its default mode, with LST
 253 data from NASA MODIS onboard Aqua product (MYD21). The LST acquisition time of
 254 MODIS Aqua is 13.30 hrs local time and daily LST of MYD21 product (MYD21A1D) was used
 255 in the present analysis. In both configurations, STIC1.2 and CLM5.0 used the same atmospheric
 256 forcing preprocessed using the FLUXNETLSM v.1.0 R package (Ukkola et al., 2017). The
 257 results of the virtual reality are exploited to get a deeper understanding of the link between LST,
 258 D_a , and the land surface energy partitioning in the diagnostic (STIC1.2) and prognostic
 259 (CLM5.0) models. This link is explained through the analysis of the ratio between the stomata
 260 and aerodynamic conductance from both STIC1.2 and CLM5.0 and their controlling
 261 environmental drivers. The analysis of the results is consistently performed using the water stress
 262 factor of CLM5.0 (β) as a third variable to understand the agreement/disagreements between the
 263 conductances and fluxes from the two models for a wide range of atmospheric and plant water
 264 stress conditions. Furthermore, Partial Least Squares Regression (PLSR) is employed to identify
 265 fundamental relationships between the individual conductances and a host of model input
 266 variables. Regressions are made using the SIMPLS algorithm, which calculates PLS factors
 267 directly as linear combinations of the original variables (de Jong, 1993; Trebs et al., 2021) after
 268 normalization of all variables. To understand the degree of relationship between the input
 269 variables and the conductances, we derived the Variable Importance in Projection (VIP) scores
 270 based on the normalized PLS weights, scores, and loadings according to Trebs et al. (2021). A
 271 conceptual diagram of the virtual reality framework and the nature of the analysis is presented in
 272 Figure 1.

273 Three statistical metrics were used to assess the performances of LST, and latent and
 274 sensible heat flux:

$$r = \frac{\sum_{i=1}^n (E_i - \bar{E})(O_i - \bar{O})}{\sqrt{\sum_{i=1}^n (E_i - \bar{E})^2} \sqrt{\sum_{i=1}^n (O_i - \bar{O})^2}}$$

$$RMSD = \sqrt{\sum_{i=1}^n \frac{(E_i - O_i)^2}{n}}$$

$$bias = \sum_{i=1}^n \frac{E_i - O_i}{n}$$

275 where r is the Pearson's correlation coefficient, $RMSD$ is root-mean-square difference, $bias$ is the
 276 mean bias, between the model and measurements, n is the total number of data pairs. E_i and O_i are
 277 the model estimated and measured fluxes and \bar{E} is the average of measured values and \bar{O} is the average
 278 of estimated values. Additionally, the Kling-Gupta efficiency (KGE) is adopted to provide a
 279 quantitative and objective assessment of the agreement between the measured (virtual reality) and
 280 estimated surface energy balance fluxes (Gupta et al. 2009). It is calculated as follows:

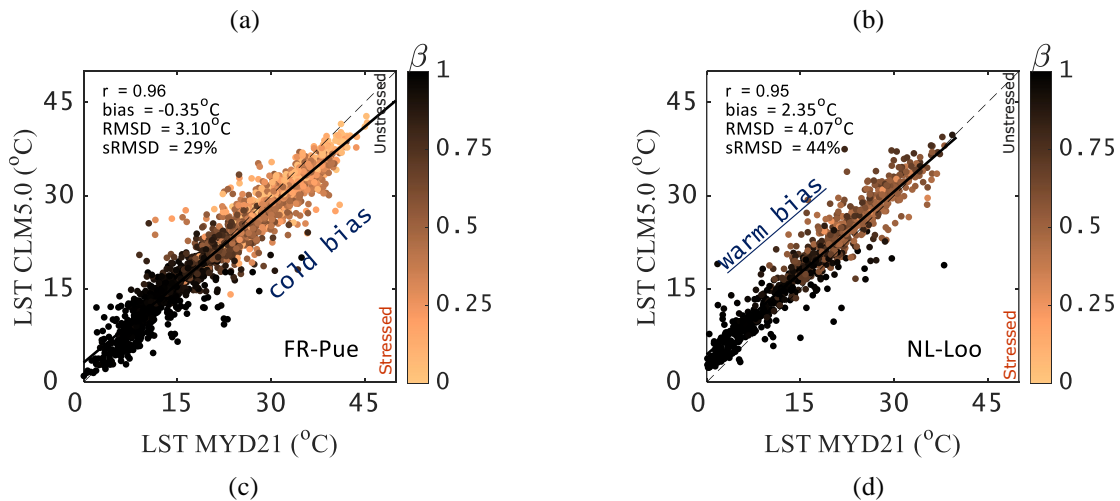
$$KGE = 1 - \sqrt{(r - 1)^2 + \left(\frac{\sigma_E}{\sigma_0} - 1\right)^2 + \left(\frac{\bar{E}}{\bar{O}} - 1\right)^2}$$

281 where r is the Pearson correlation coefficient, σ_0 and σ_E are the standard deviations of virtual reality
 282 and STIC1.2 estimates, respectively. The closer KGE is to 1, the more consistent are the STIC1.2
 283 estimates with respect to the virtual reality.

284 3 Results and Discussion

285 3.1 Comparing CLM5.0 and MYD21A1D LST and SEB fluxes for a range of water stress

286 LST is one of the important boundary conditions that drives the biophysical conductances
 287 and fluxes in STIC1.2. Since CLM5.0 LST is used to drive STIC1.2 in scenario-1, a comparison
 288 of CLM5.0 LST with respect to a reference dataset is necessary. Therefore, we use the most
 289 recent version of MODIS (MODERate Resolution Imaging Spectroradiometer) on-board Aqua
 290 daily LST product (product name MYD21) as a reference data for such a comparison. LST
 291 estimates from CLM5.0 were significantly correlated ($r = 0.95 - 0.96$, $p < 0.05$) with MYD21
 292 retrievals (**Figure 2a - b**) for the simulated ranges of β , with a bias and systematic root mean
 293 square difference (sRMSD) of $-0.35 - 2.35^\circ\text{C}$ and $29 - 44\%$, respectively. While cold bias in
 294 CLM5.0 for $LST > 25^\circ\text{C}$ corresponded to high soil and atmospheric water stress in the model (β :
 295 $0 - 0.25$) in FR-Pue, a consistent warm bias in CLM5.0 LST was also evident for the entire range
 296 of β in NL-Loo.



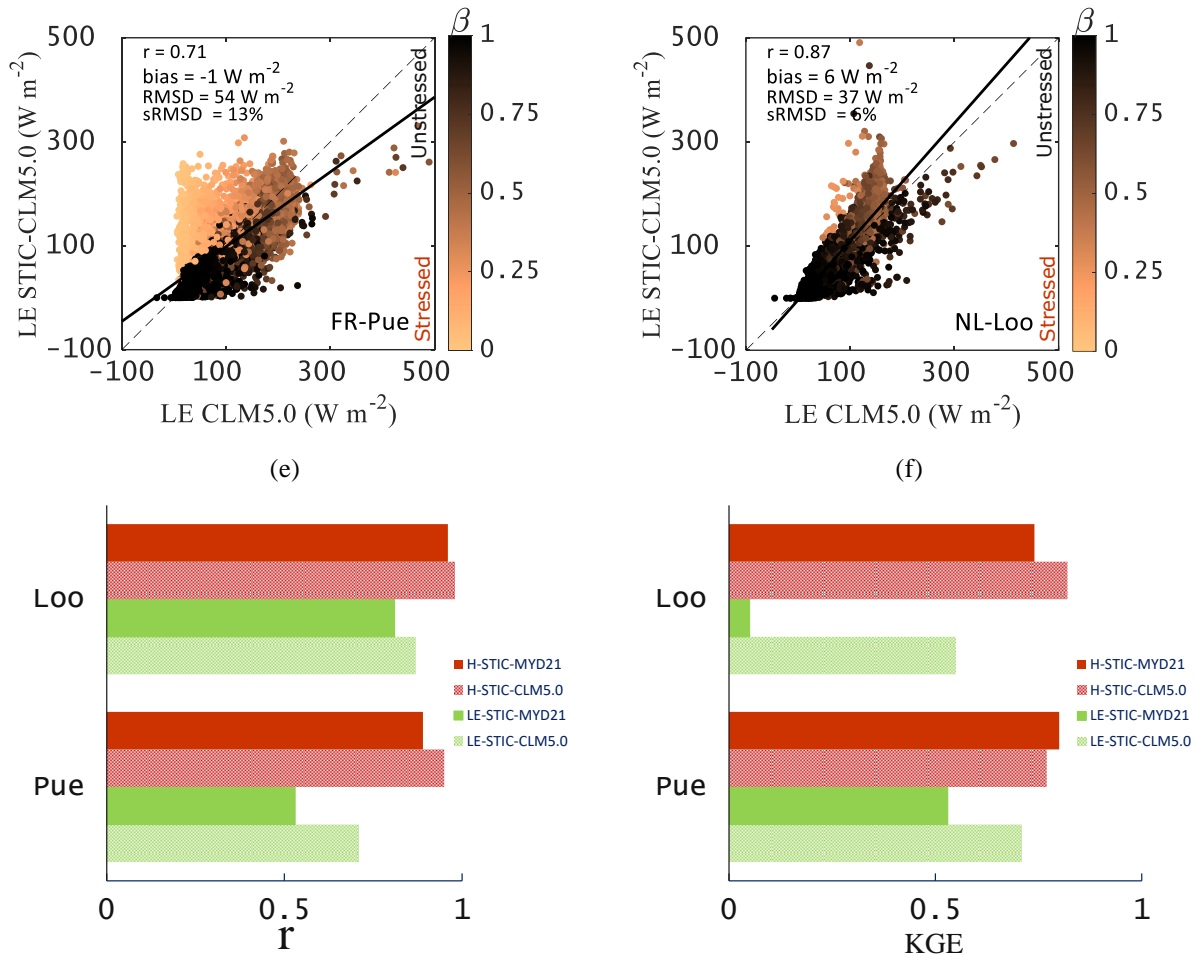


Figure 2. (a) – (b) Evaluation of CLM5.0 simulated LST with respect to MYD21 LST product in FR-Pue and NL-Loo for a range of CLM5.0 simulated beta factor (β); (c) – (d) Comparison between STIC1.2 simulated LE with respect to the virtual reality (scenario-1) for a range of CLM5.0 simulated beta factor (β); (e) – (f) Comparison of correlation and KGE statistics of LE and H between scenario-1 and scenario-2.

297 Like LST, comparison of surface energy balance fluxes between CLM5.0 and STIC1.2
 298 was also made for the entire range of β . Comparison of LE between CLM5.0 and virtual
 299 STIC1.2 (STIC1.2-CLM5.0) (scenario-1) showed significant correlation between them ($r = 0.71$
 300 $- 0.86$, $p < 0.05$) in both the sites, with sRMSD and KGE of 6 – 13% and 0.55 – 0.71 (Figure 2c –
 301 d; Figure 2e – f). However, the correlation and KGE statistics of LE was degraded ($r = 0.53$ –
 302 0.81 ; KGE: 0.05 – 0.53) when STIC1.2 was forced with MYD21 LST (STIC1.2-MYD21)
 303 (scenario-2). Interestingly, the two models showed stronger agreement for H as compared to LE
 304 in scenario-1 and scenario-2 in both the sites. In scenario-1, a significant correlation of 0.95 –
 305 0.98 ($p < 0.05$) (Figure S1 in Supporting Information), sRMSD of 36 – 44%, and KGE 0.77 –
 306 0.82 (Figure 2e – f) was found. Like LE, the correlation and KGE statistics of H also degraded (r
 307 $= 0.89$ – 0.96 ; KGE: 0.74 – 0.80) when STIC1.2 was forced with MYD21 LST (STIC1.2-
 308 MYD21) (scenario-2). There are two aspects in these results that are worth highlighting. It is
 309 evident that in scenario-1, the same LST conditions produced different LE and H in CLM5.0 and
 310 STIC1.2-CLM5.0. This is because CLM5.0 and STIC1.2-CLM5.0 formulate the water stress in

311 different ways. In STIC1.2, the water stress factor (I_{sm}) is calculated as an inverse of aggregated
 312 wetness of canopy-soil complex (Mallick et al., 2022, 2018), which controls the transition from
 313 potential to actual evaporation. This implies that $I_{sm} \rightarrow 1$ on the unstressed surface and $I_{sm} \rightarrow 0$ on
 314 the stressed surface. Therefore, I_{sm} is critical for providing a constraint against which the
 315 conductances are estimated. In STIC1.2-CLM5.0, the simulated LST from CLM5.0 is directly
 316 used for estimating I_{sm} in conjunction with air and dewpoint temperatures by exploiting the
 317 psychrometric theory of vapor pressure-temperature slope relationship (details in Mallick et al.,
 318 2022). In CLM5.0, the β -factor is estimated based on the simulated leaf water potential of the
 319 plant hydraulic system following a sigmoidal function accounting for the water potential at 50%
 320 loss of stomata conductance and a shape-fitting parameter (Kennedy et al., 2019). These two
 321 structurally different ways of formulating plant water stress tend to produce different water stress
 322 conditions in the two sites under the same LST. For a detailed investigation, a comparison
 323 between I_{sm} versus β is shown in the scatterplots in Supporting Information (**Figure S2a, b**). In
 324 FR-Pue, relatively less stressed conditions in STIC1.2 (i.e., $I_{sm} > \beta$) was evident with increasing
 325 LST (from 20 – 30 °C), part of which also coincided with high D_a ($D_a > 30$ hPa) (datapoints
 326 above zero-line in **Figure S2** in the Supporting Information document). These conditions tend to
 327 produce an overestimation of LE in STIC1.2 in the scenario-1 despite it is virtually stressed
 328 ($\beta < 0.3$). On the other side, relatively more stressed conditions in STIC1.2 (i.e., $I_{sm} < \beta$) for a
 329 wide range of D_a values was also visible at both sites (datapoints below zero-line in **Figure S2** in
 330 the Supporting Information). This is more evident in NL-Loo where β simulated by CLM5.0 is
 331 systematically larger (i.e., close to unstressed) than its counterpart in STIC1.2 (i.e., I_{sm}) for the
 332 entire range of LST values. In addition, the comparison of the simulated energy fluxes and the β
 333 factor across the two scenarios (i.e., CLM5.0 LST vs. MYD21 LST) and the two selected sites
 334 (i.e., FR-Pue vs. NL-Loo) allow to better assess the relative role of LST on SEB in the diagnostic
 335 and prognostic models. For example, in **Figure 2f**, LE at NL-Loo revealed distinct differences
 336 between STIC1.2-CLM5.0 and STIC1.2-MYD21. This is the site where consistent positive bias
 337 was found between CLM5.0 and MYD21 LST, however the relative difference in the water
 338 stress factor simulated by the two models does not drastically change between scenario-1 and
 339 scenario-2 (see **Figure S2c, d**).

340 Finally, it is also important to highlight that larger LE fluxes simulated by STIC1.2-
 341 CLM5.0 under soil and atmospheric drought conditions are associated with more stress
 342 conditions at the ecosystem scale. In addition to the water stress, the differences in stomatal and
 343 aerodynamic conductance formulation in the two models might also have produced different
 344 conductances values and the results are consequently reflected on the surface energy balance
 345 fluxes. While a cold (warm) LST bias during high water stress increases the likelihood
 346 possibility of unstressed (stressed) stomatal conductance simulation through STIC1.2, it
 347 simultaneously increases the possibility of a low (high) aerodynamic conductance simulation as
 348 well, ultimately leading to substantial differences in LE and H response to soil and atmospheric
 349 drought conditions. Thus, all these different aspects suggest a further analysis of the simulated
 350 biophysical conductances in both STIC1.2 and CLM5.0 to gain further insight on the explanation
 351 of the response of the two models to soil and atmospheric drought.

352 3.2 Biophysical conductances

353 The biophysical conductance (g_{cs}/g_a ratio) from STIC1.2-CLM5.0 appeared to be
 354 significantly correlated with CLM5.0 in FR-Pue ($r = 0.75$) across the entire range of β (scenario-
 355 1) (**Figure 3a**). However, profound differences in g_{cs}/g_a between STIC1.2-CLM5.0 and CLM5.0

356 was evident with rising soil and atmospheric drought (β : 0 – 0.25), which also corresponded with
 357 high magnitude of LST ($>35^{\circ}\text{C}$) and D_a (>30 hPa) (**Figure 3a**). Similarly, the retrieved
 358 conductances from STIC1.2-MYD21 (scenario-2) also showed significant correlation ($r = 0.68$)
 359 yet marked difference with CLM5.0 (g_{cs}/g_a STIC1.2-MYD21 $>$ g_{cs}/g_a CLM5.0) was evident
 360 (**Figure 3b**). In NL-Loo, analysis of the conductance ratio also revealed very similar pattern and
 361 substantial differences in the magnitude of g_{cs}/g_a between STIC1.2 and CLM5.0 for both the
 362 scenarios, with a relatively better correlation in scenario-1 ($r = 0.63$) as compared to scenario-2 (r
 363 $= 0.54$).
 364

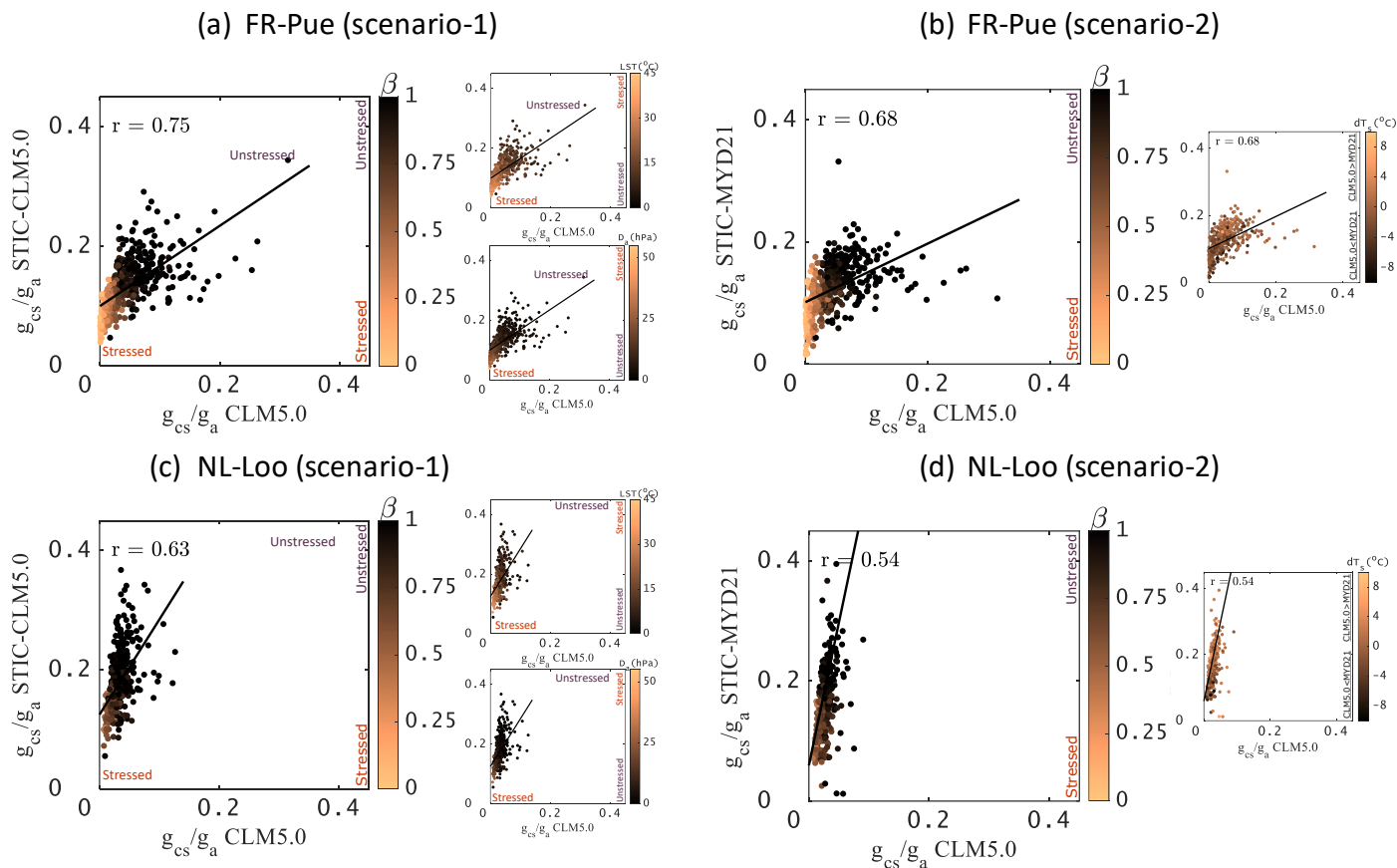


Figure 3. Scatterplots showing how the relationship and magnitude of the biophysical conductance ratios between STIC1.2 and CLM5.0 varies with different LST for a range of CLM5.0 water stress (β) in two different scenarios in FR-Pue (**a** and **b**) and NL-Loo (**c** and **d**).

365 Interestingly in both the sites, the difference in LST between CLM5.0 and MYD21 LST
 366 appeared to have small effects on differences in conductance ratios between CLM5.0 and
 367 STIC1.2. Some counter intuitive patterns also emerged out with respect to the behavior of g_{cs}/g_a
 368 with the coalition of soil and atmospheric drought (i.e., β) and LST. For example, in FR-Pue,
 369 CLM5.0 simulated colder LST as compared to MYD21 for $LST > 25^{\circ}\text{C}$, which is associated with
 370 high soil and atmospheric water stress in CLM5.0 (low β) (**Figure 2a, 3b**). Therefore, β from
 371 CLM5.0 is expected to be high (low water stress) and g_{cs}/g_a ratio from CLM5.0 is expected to
 372 show higher magnitude as compared to STIC1.2 in the scenario-2. This implies that although the
 373 conductances in CLM5.0 are sensitive to β simulation, both are somewhat less linked to the LST

374 simulation in the model. In a similar manner, despite predominantly low soil and atmospheric
 375 water stress in NL-Loo ($\beta > 0.60$, LST: 10 – 15°C, D_a : 5 – 15 hPa), CLM5.0 showed very low
 376 g_{cs}/g_a ratio as compared to STIC1.2 (**Figure 3c**). This insensitivity in CLM5.0 is presumably
 377 generated by the loose coupling of surface energy balance to the plant hydraulics
 378 parameterization used in the model to calculate the stress factor.

379

380 To probe into the reasons on substantial differences in the conductance ratios between
 381 STIC1.2 and CLM5.0, and to understand the reasons for their different sensitivity to changes in
 382 LST, we further analyzed the response of the individual conductance components (g_{cs} and g_a) to
 383 soil and atmospheric drought proxies under scenario-1. Given stomatal conductance has a strong
 384 dependence on humidity deficit (Monteith, 1995), we used vapor pressure deficit to represent
 385 atmospheric drought proxy. Due to the strong connection of LST-air temperature difference (dT_{s-a})
 386 with vegetation water stress and sensible heating (Anderson et al., 2007), we used dT_{s-a} to
 387 represent soil drought proxy (**Figure 4**).

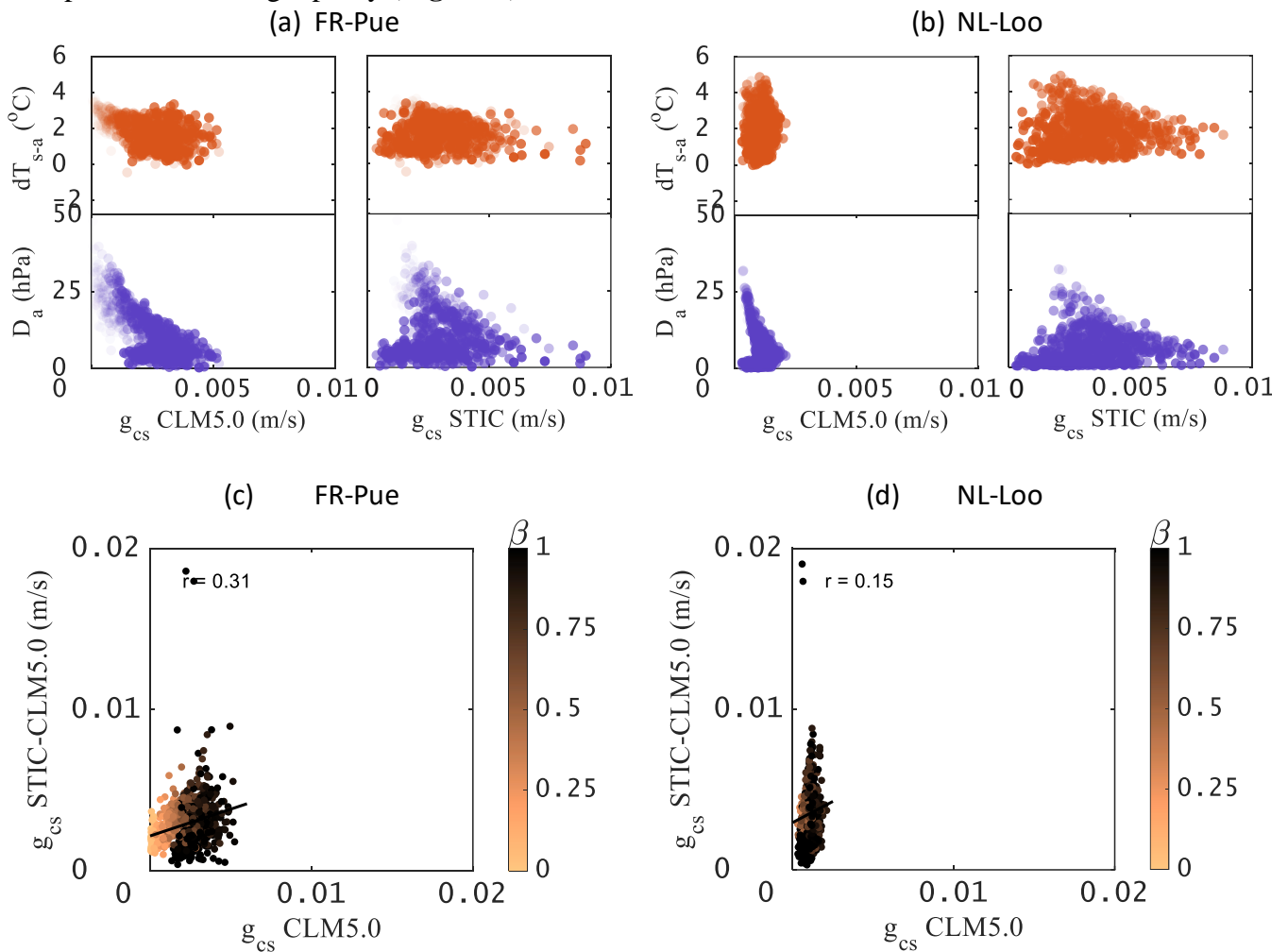


Figure 4. Response of retrieved g_{cs} to LST air temperature difference (dT_{s-a}) and atmospheric vapor pressure deficit (D_a) representing soil and atmospheric drought proxy, respectively, for (a) FR-Pue and (b) NL-Loo. Comparison between STIC1.2-derived g_{cs} and CLM5.0 g_{cs} for a broad spectrum of water stress simulated by CLM5.0.

388

389 In both FR-Pue and NL-Loo, CLM5.0 showed a non-linear reduction in g_{cs} with
 390 increasing D_a and reached an asymptotic decline afterwards (**Figure 4a – b**), which is a sign of a
 391 typical negative feedback. This control of atmospheric humidity deficit on stomatal action is
 392 subsequently modified by surface temperature feedback. A reduced transpiration due to partial
 393 stomatal closure can increase the surface temperature, which affects LST and the saturation
 394 vapor pressure at the vegetation surface. A negative temperature control loop is evident in FR-
 395 Pue where g_{cs} also declined with dT_{s-a} . However, no temperature control was found in NL-Loo,
 396 presumably due to mostly unstressed condition (high β) generated in CLM5.0. This unstressed
 397 condition is driven by a large soil water reservoir in NL-Loo reaching more than 30 m depth, in
 398 contrast with the soil depth of less than 1 m in FR-Pue. Finally, the narrow range of g_{cs} values
 399 simulated by CLM5.0 in NL-Loo, despite the favorable environmental conditions at the site
 400 compared to FR-Pue, is due to the stomatal conductance parameter value (i.e., g_1), which is by
 401 default equal to 2.35 for needleleaf evergreen temperate species (4.45 for broadleaf evergreen
 402 trees in FR-Pue). However, very surprisingly the magnitude of LE differed much less than as
 403 compared to g_{cs} between these two sites. For instance, in NL-Loo, CLM5 produced almost
 404 similar magnitude of LE as FR-Pue while having substantially lower g_{cs} as compared to FR-Pue.
 405 On the contrary, the scatterplot of g_{cs} versus D_a in STIC1.2 showed relatively complex pattern
 406 between atmospheric drought and g_{cs} , pointing towards feedback response (**Figure 4a – b**). Such
 407 type of feedback occurs when a change in evaporation causes a change in the conductance which
 408 subsequently affects the evaporation rate (Monteith, 1995). We found low g_{cs} in STIC1.2 at
 409 highest D_a because large humidity deficits strictly restrict water loss under high water stress. g_{cs}
 410 was also low at lowest D_a because of saturation and low humidity deficit. Conductance was
 411 optimum at intermediate D_a and evaporation. Due to the very different responses of g_{cs} to D_a in
 412 CLM5.0 and STIC1.2, the relationship between the two g_{cs} was poor in both the sites and their
 413 absolute values also differed across the entire range of β (**Figure 4c – d**). This further
 414 emphasizes the fact that there is no universal function of stomatal conductance to atmospheric
 415 vapor pressure deficits and different ecosystems have different sensitivity of stomatal
 416 conductance to environmental variables. The similar principle also applies for the stomatal
 417 response function to soil drought.

418 Analysis of aerodynamic conductance (g_a) revealed very similar behavior of g_a with
 419 respect to the response of g_a to D_a and dT_{s-a} both in CLM5.0 and STIC1.2 (Figure 5a, 5b). In
 420 both the sites, a logarithmic response of g_a to D_a was evident in both the models, where g_a
 421 increased with increasing D_a and became asymptotic after D_a exceeded 25 hPa. The pattern of
 422 dT_{s-a} versus g_a was linear to exponential in both the models. However, marked differences in the
 423 magnitude of g_a between CLM5.0 and STIC1.2 was found in FR-Pue, although significantly high
 424 correlation between the two g_a estimates was found in both the sites ($r = 0.75 - 0.80$). The
 425 differences in absolute magnitude of g_a between the two models is presumably due to the
 426 differences in the model structure. While g_a estimation in CLM5.0 is based on the Monin-
 427 Obukhov Similarity Theory involving corrections due to atmospheric stability, parameterization
 428 of surface roughness lengths, estimation of g_a in STIC1.2 is based on LST and environmental
 429 variables without involving any atmospheric sub-models. However, the significant correlation
 430 between the two g_a estimates and their responses to soil/atmospheric drought metrics signifies
 431 the need of unified and common approach of aerodynamic conductances in both prognostic and
 432 diagnostic models to understand the differences in surface energy balance flux prediction. A
 433 possible solution to address this challenge could be the implementation of data-driven techniques

434 for the calculation of both g_a and g_{cs} (e.g., ElGhawi et al., 2023) in both prognostic and
 435 diagnostic approaches for modelling evapotranspiration.
 436

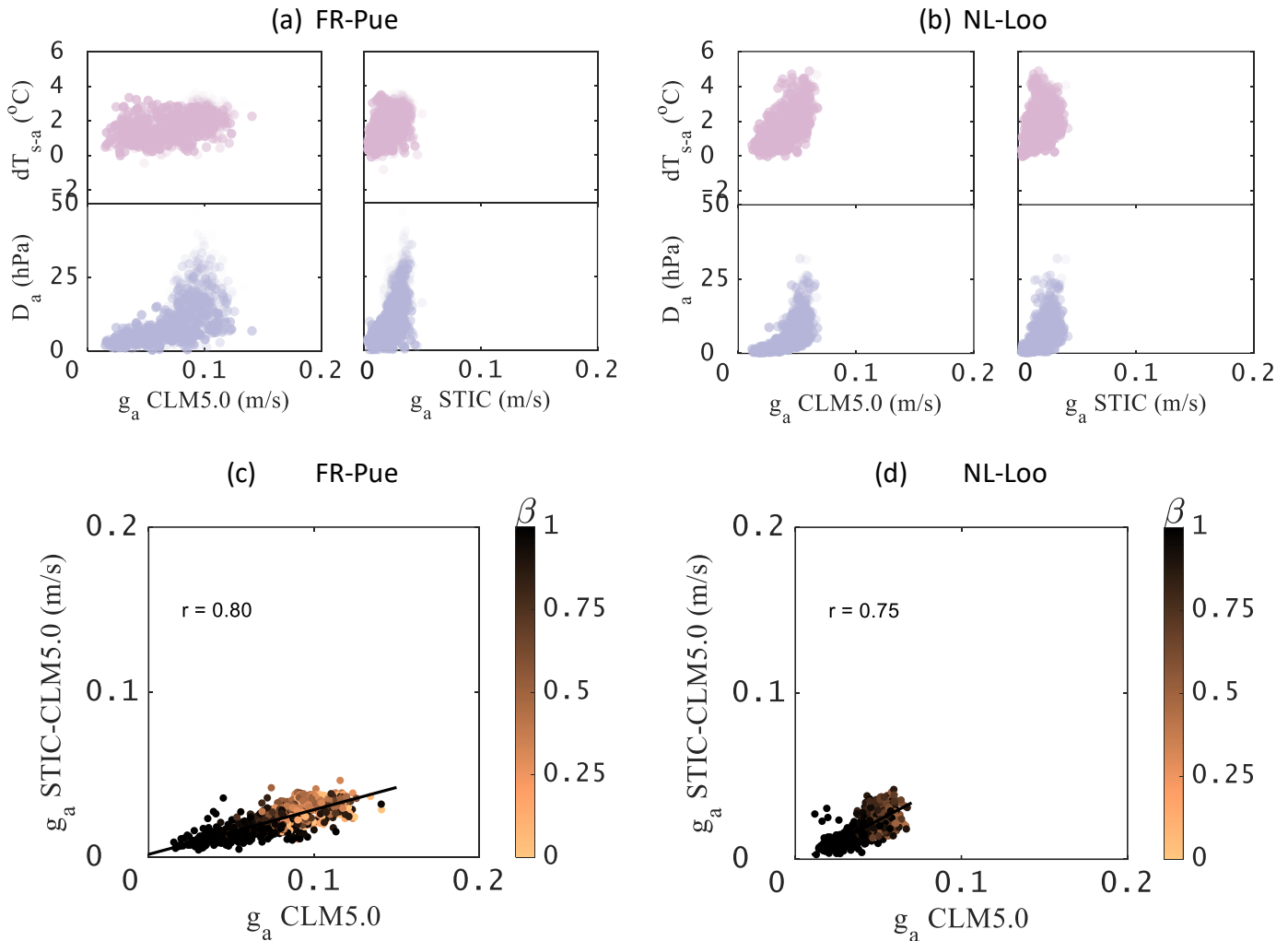


Figure 5. Response of retrieved g_a to LST air temperature difference (dT_{s-a}) and atmospheric vapor pressure deficit (D_a) representing soil and atmospheric drought proxy, respectively, for (a) FR-Pue and (b) NL-Loo. Comparison between STIC1.2-derived g_a and CLM5.0 g_a for a broad spectrum of water stress simulated by CLM5.0 for (c) FR-Pue and (d) NL-Loo.

437

438 3.3 Factor controlling conductances and fluxes in the models

439 To substantiate our findings from the previous sections, we further investigated the
 440 relationship of the individual conductances and surface energy balance fluxes as final model
 441 output with a host of environmental and surface variables by performing a partial least square
 442 regression (PLSR) analysis for the scenario-1 (**Figure 6**). If the Variable Importance in
 443 Projection (VIP) score exceeds a value of 0.8, the variable is considered to play an important role
 444 in determining the magnitude and variability on g_a , g_{cs} , LE and H, respectively (Trebs et al.,
 445 2021).

446

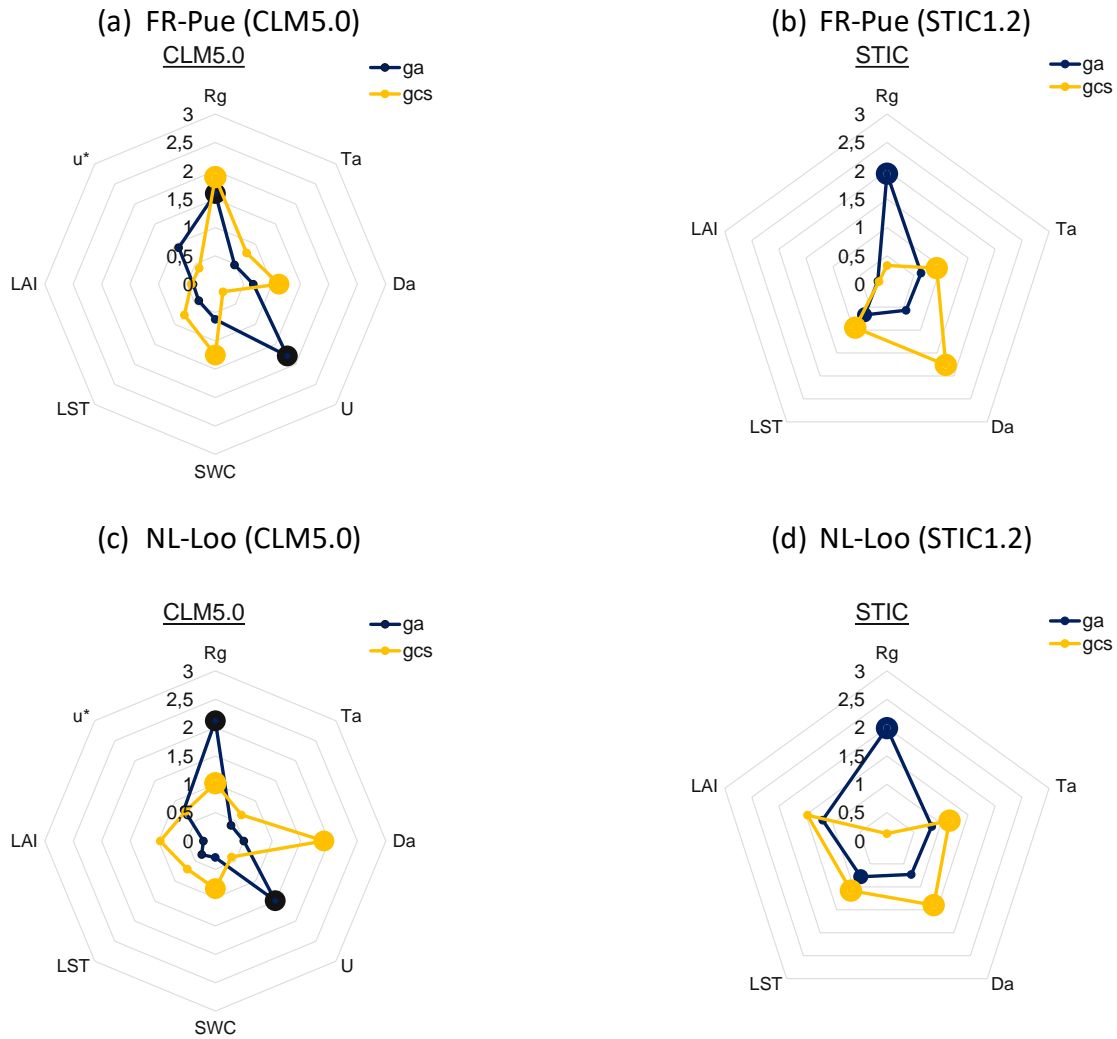


Figure 6. Radar charts of the Variable Importance in Projection (VIP) scores for aerodynamic and canopy-stomatal conductance (g_a and g_{cs}) estimated from CLM5.0 and STIC1.2 with respect to environmental, hydrological and land surface variables for both FR-Pue and NL-Loo. Here R_g is the shortwave radiation, T_a is the air temperature, D_a is the atmospheric vapor pressure deficit, U is the wind speed, SWC is the soil water content, LST is the land surface temperature, LAI is the leaf area index, and u^* is the friction velocity, respectively.

447 The results from the PLSR analysis indicated that for CLM5.0, while the shortwave
 448 radiation (R_g) and wind speed (U) has a major impact on the aerodynamic conductance, the g_{cs} is
 449 mainly regulated by R_g , D_a and simulated soil water content (SWC) in both the sites. Whereas
 450 for STIC1.2, while the effects of R_g and LST was maximum on g_a , the variations in g_{cs} were
 451 maximally impacted by LST , D_a and air temperature (T_a), respectively. The influence of R_g on
 452 the modeled g_{cs} in STIC1.2 apparently had minor importance. This could be due the fact that the
 453 effects of R_g is already accounted in the air temperature signal and no additional effects of R_g
 454 was noted. On the other hand, the large influence of R_g to g_{cs} in CLM5.0 could presumably be
 455 explained by the coupled photosynthesis-stomata conductance model where photosynthetically
 456 active radiation is directly used to solve the system of equations for sunlit and shaded leaves.

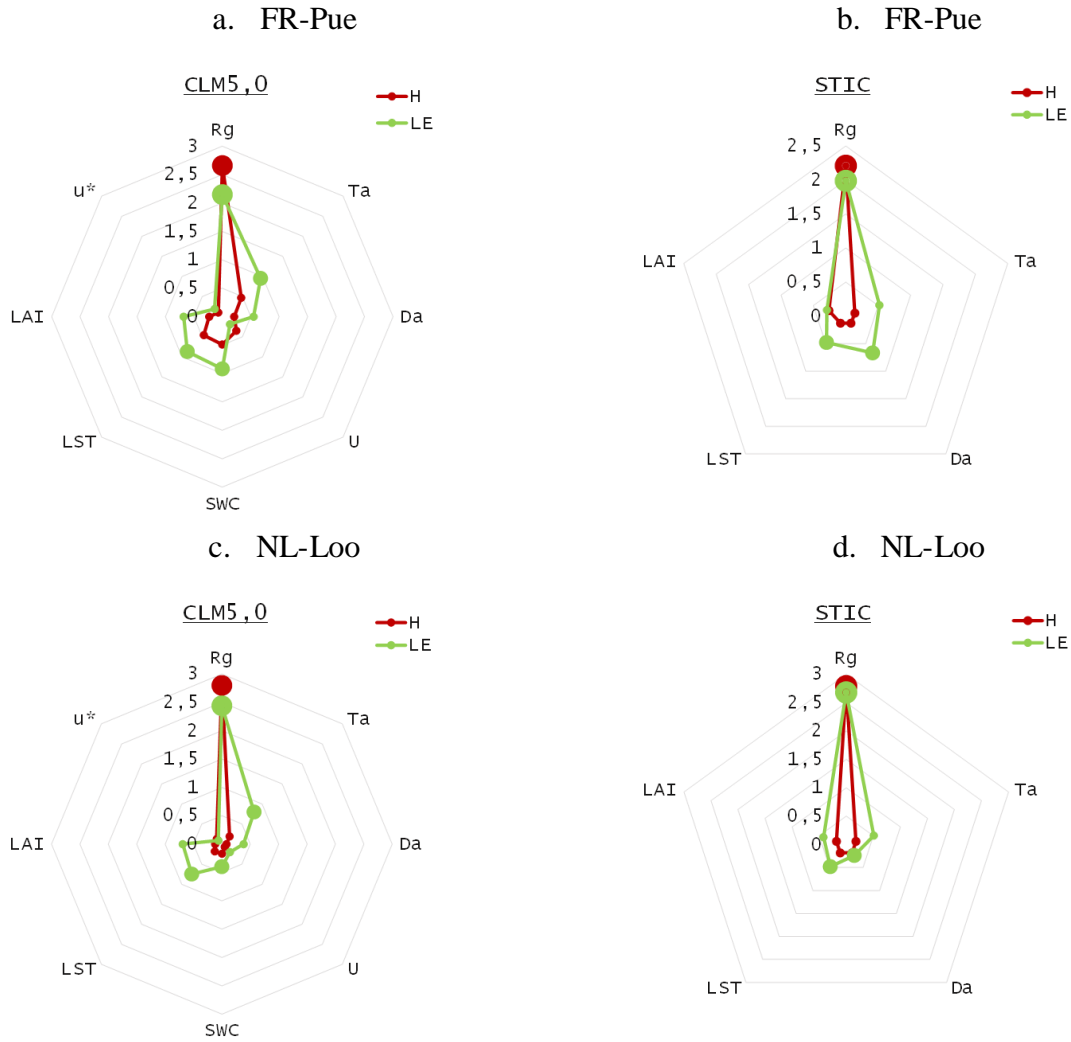


Figure 7. Radar charts of the Variable Importance in Projection (VIP) scores for latent and sensible heat fluxes (LE and H) estimated from CLM5.0 and STIC1.2 with respect to environmental, hydrological and land surface variables for both FR-Pue and NL-Loo. Here R_g is the shortwave radiation, T_a is the air temperature, D_a is the atmospheric vapor pressure deficit, U is the wind speed, SWC is the soil water content, LST is the land surface temperature, LAI is the leaf area index, and u^* is the friction velocity, respectively.

457

458

459

460

461

462

463

464

465

466

Another interesting feature emerging from the VIP analysis is the relatively stable importance of D_a in STIC1.2 to explain g_{cs} response across the two sites. In CLM5.0, the importance of D_a clearly increases in NL-Loo due to the marginal role played by SWC due to continuous supply of plant available water in this ecosystem. Finally, both STIC1.2 and CLM5.0 show an increasing importance of LAI to explain g_{cs} when moving from broadleaf evergreen trees (i.e., FR-Pue) to needleleaf evergreen trees (i.e., NL-Loo).

Similar analysis with the surface energy balance fluxes indicated that for CLM5.0, while R_g has the major impact on the sensible heat flux; R_g , T_a , SWC , and simulated LST was found to

467 have substantial control on the variability in LE in both the sites. For STIC1.2, despite the same
468 pattern was found for sensible heat flux, however, the variability of LE was significantly
469 controlled by R_g , D_a , and LST. It is also worth mentioning that the effects of the environmental
470 variables were substantially stronger on the conductances as compared to the surface energy
471 balance fluxes. This PLSR analysis further emphasizes the fact that for using model and satellite-
472 based evaporation as a water cycle predictor, we not only need to capture the magnitude and
473 variability of the biophysical conductances, but we need consensus models that will explain the
474 effects of complex coalition of soil and atmospheric drought on the conductances. However, this
475 is a non-trivial problem and too often such complexities are tackled with over simplified or over-
476 parameterized models involving too many calibrations that do not consider the interactions and
477 feedbacks (whether negative or feedforward) that are observed in nature.

478 **5 Conclusions and Future Implications**

479 The study critically evaluates the evaporation response and the inherent biophysical
480 conductances, namely stomatal and aerodynamic, simulated by a diagnostic non-parametric
481 thermal remote sensing model (i.e., STIC1.2) and by a prognostic state-of-the-art land surface
482 model (i.e., CLM5.0). We implemented a virtual reality experimental framework to understand
483 the conjugate effects of soil and atmospheric drought on the response of these two conductances
484 that have significant impact in modulating evaporation. In this framework, the two models share
485 the same upper (i.e., atmospheric) and lower (i.e., land surface temperature) boundary
486 conditions. An extended analysis on the comparison of the conductances and fluxes based on
487 soil-atmospheric water stress factor led us to the following conclusion and the emergent future
488 implications:

- 489 a) Despite the relatively good agreement in the simulated surface energy balance fluxes, the
490 two models show substantial divergence in reproducing the magnitude and variability of
491 the aerodynamic and stomatal conductances. This divergence is explained by the
492 structural differences in the formulation of plant water stress in two different models,
493 which tend to produce very different water stress conditions in two contrasting forest
494 sites despite the two models had the same land surface temperature and vapor pressure
495 deficit conditions.
- 496 b) Analysis of the individual biophysical conductances revealed that the profound
497 differences in the magnitude and response of stomatal and aerodynamic conductance was
498 not only associated with the water stress factor, but also due to different functional
499 representation of the individual conductances in two different models. The differences in
500 the functional representation led to very different response of the aerodynamic and
501 stomatal conductances to soil and atmospheric drought in the models.
- 502 c) The magnitude and variability of the aerodynamic conductance of CLM5.0 is largely
503 explained by wind speed and solar radiation across the two selected sites, while in
504 STIC1.2 it is mainly influenced by solar radiation and a larger host of variables including
505 D_a , LST, and T_a . On the other hand, the magnitude and variability of stomatal
506 conductance is explained by solar radiation, D_a , and soil water content in CLM5.0, and
507 by D_a , T_a , and LST in STIC1.2.
- 508 d) The substantial differences in water stress estimation and in the biophysical conductances
509 led to differences in evaporative flux estimates of CLM5.0 and STIC1.2. These
510 differences are larger for LE and for the more humid site of NL-Loo.

511 Our study results have important implications for both the remote sensing and the land surface
 512 community, highlighting the need for an in-depth comparison of different modelling approaches
 513 to understand their biases and uncertainty. More specifically, the findings of our work suggest
 514 the need of a unified approach in the treatment of the biophysical conductances with respect to
 515 their responses to water stress in the two very diverse modelling community for achieving a
 516 more robust multi-model assessment of the evaporation fluxes.
 517

518 **Acknowledgments**

519 This work was supported by the Luxembourg National Research Fund (FNR) CORE
 520 program (C19/SR/13652816/CAPACITY). KM also acknowledges the financial support of the
 521 FNR INTER MOBILITY program (INTER/MOBILITY/2020/14521920/MONASTIC). TH was
 522 supported by the European ECOSTRESS Hub project (EEH, Contract No. 4000129873/20/I-
 523 NS), funded by the European Space Agency (ESA).
 524

525 **Open Research**

526 The FLUXNET data used for atmospheric forcing in the study are available at
 527 <https://fluxnet.org/data/fluxnet2015-dataset>. CLM5.0 is publicly available through the
 528 Community Terrestrial System Model (CTSM) git repository (Tag name: release-clm5.0.30) via
 529 <https://github.com/ESCOMP/ctsm> (CTSM, 2017/2022). The results of the numerical
 530 experiments and Matlab scripts used for the data analysis of this manuscript are available at
 531 ZENODO repository via <https://doi.org/10.5281/zenodo.8318671>.
 532

533 **References**

- 534 Anderson, M. C., Norman, J. M., Mecikalski, J. R., Otkin, J. A., & Kustas, W. P. (2007). A
 535 climatological study of evapotranspiration and moisture stress across the continental United
 536 States based on thermal remote sensing: 2. Surface moisture climatology. *Journal of Geophysical*
 537 *Research: Atmospheres*, 112(D11). <https://doi.org/10.1029/2006JD007507>
- 538 Anderson, M., Kustas, W., Alfieri, J., Gao, F., Hain, C., Prueger, J., Evett, S., Colaizzi, P.,
 539 Howell, T. & Chávez, J. (2012). Mapping daily evapotranspiration at Landsat spatial scales
 540 during the BEAREX'08 field campaign. *Advances in Water Resources*. 50, 162 – 177,
 541 <https://doi.org/10.1016/j.advwatres.2012.06.005>
- 542 Bhattarai, N., Mallick, K., Brunzell, N. A., Sun, G., & Jain, M. (2018). Regional
 543 evapotranspiration from an image-based implementation of the Surface Temperature Initiated
 544 Closure (STIC1. 2) model and its validation across an aridity gradient in the conterminous US.
 545 *Hydrology and Earth System Sciences*, 22(4), 2311-2341. [https://doi.org/10.5194/hess-22-2311-](https://doi.org/10.5194/hess-22-2311-2018)
 546 2018
- 547 Bhattarai, N., Mallick, K., Stuart, J., Vishwakarma, B. D., Niraula, R., Sen, S., & Jain, M.
 548 (2019). An automated multi-model evapotranspiration mapping framework using remotely
 549 sensed and reanalysis data. *Remote Sensing of Environment*, 229, 69-92.
 550 <https://doi.org/10.1016/j.rse.2019.04.026>
- 551 Beck, H. E., Zimmermann, N. E., McVicar, T. R., Vergopolan, N., Berg, A., & Wood, E.
 552 F. (2018). Present and future Köppen-Geiger climate classification maps at 1-km resolution,
 553 *Scientific data*, 5, 1–12. <https://doi.org/10.1038/sdata.2018.214>
- 554 Byrne, M. P., & O'Gorman, P. A. (2013). Link between land-ocean warming contrast and
 555 surface relative humidities in simulations with coupled climate models. *Geophysical Research*
 556 *Letters*, 40(19), 5223-5227. <https://doi.org/10.1002/grl.50971>

- 557 Chen, Y., K. Yang, D., Zhou, Qin, J., & Guo, X. (2010). Improving the Noah land surface
558 model in arid regions with an appropriate parameterization of the thermal roughness length.
559 *Journal of Hydrometeorology*, 11(4), 995–1006. <https://doi.org/10.1175/2010JHM1185.1>
- 560 Chen, L., Dirmeyer, P.A. (2020). Reconciling the disagreement between observed and
561 simulated temperature responses to deforestation. *Nature Communications*. 11(1), 202.
562 <https://doi.org/10.1038/s41467-019-14017-0>
- 563 Cabon, A., Mouillot, F., Lempereur, M., Ourcival, J.-M., Simioni, G., & Limousin, J.-M.
564 (2018). Thinning increases tree growth by delaying drought-induced growth cessation in a
565 Mediterranean evergreen oak coppice. *Forest Ecology and Management*, 409, 333-
566 342. <https://doi.org/10.1016/j.foreco.2017.11.030>
- 567 Damour, G., Simonneau, T., Cochard, H., & Urban, L. (2010). An overview of models of
568 stomatal conductance at the leaf level. *Plant, cell & environment*, 33(9), 1419-1438.
569 <https://doi.org/10.1111/j.1365-3040.2010.02181.x>
- 570 de Jong, S. (1993). SIMPLS: an alternative approach to partial least squares regression.
571 *Chemometrics and Intelligent Laboratory Systems*, 18(3), 251-263. [https://doi.org/10.1016/0169-](https://doi.org/10.1016/0169-7439(93)85002-X)
572 [7439\(93\)85002-X](https://doi.org/10.1016/0169-7439(93)85002-X)
- 573 ElGhawi, R., Kraft, B., Reimers, C., Reichstein, M., Körner, M., Gentine, P., & Winkler,
574 A. J. (2023). Hybrid modeling of evapotranspiration: inferring stomatal and aerodynamic
575 resistances using combined physics-based and machine learning. *Environmental Research*
576 *Letters*, 18(3). <https://doi.org/10.1088/1748-9326/acbbe0>
- 577 Gao, Z., N. Chae, J., Kim, J., Hong, T. Choi, & Lee H. (2004). Modeling of surface energy
578 partitioning, surface temperature, and soil wetness in the Tibetan prairie using the Simple
579 Biosphere Model 2 (SiB2). *Journal of Geophysical Research: Atmospheres* 109, D06102,
580 <https://doi.org/10.1029/2003JD004089>
- 581 Gevaert, A. I., Miralles, D. G., de Jeu, R. A., Schellekens, J., & Dolman, A. J. (2018). Soil
582 moisture-temperature coupling in a set of land surface models. *Journal of Geophysical Research:*
583 *Atmospheres*, 123(3), 1481–1498. <https://doi.org/10.1002/2017JD027346>
- 584 Gupta, H. V., Kling, H., Yilmaz, K. K., & Martinez, G. F. (2009). Decomposition of the
585 mean squared error and NSE performance criteria: Implications for improving hydrological
586 modelling. *Journal of hydrology*, 377(1-2), 80-91. <https://doi.org/10.1016/j.jhydrol.2009.08.003>
- 587 Green, J. K., Ballantyne, A., Abramoff, R., Gentine, P., Makowski, D., & Ciais, P. (2022).
588 Surface temperatures reveal the patterns of vegetation water stress and their environmental
589 drivers across the tropical Americas. *Global Change Biology*, 28(9), 2940– 2955.
590 <https://doi.org/10.1111/gcb.16139>
- 591 Holwerda, F., Bruijnzeel, L. A., Scatena, F. N., Vugts, H. F., & Meesters A.G.C.A. (2012).
592 Wet canopy evaporation from a Puerto Rican lower montane rain forest: The importance of
593 realistically estimated aerodynamic conductance. *Journal of Hydrology*, 11, 414-415,
594 <https://doi.org/10.1016/j.jhydrol.2011.07.033>
- 595 Kennedy, D., Swenson, S., Oleson, K. W., Lawrence, D. M., Fisher, R., da Costa, A. C. L.,
596 & Gentine, P. (2019). Implementing plant hydraulics in the Community Land Model, Version 5.
597 *Journal of Advances in Modeling Earth Systems*, 11(2), 485–513.
598 <https://doi.org/10.1029/2018ms001500>
- 599 Koch, J., Siemann, A., Stisen, S., & Sheffield, J. (2016). Spatial validation of large-scale
600 land surface models against monthly land surface temperature patterns using innovative
601 performance metrics. *Journal of Geophysical Research: Atmospheres*, 121(10), 5430– 5452,
602 <https://doi.org/10.1002/2015JD024482>

- 603 Koster, R.D., Dirmeyer, P.A., Guo, Z., Bonan, G., Chan, E., Cox, P., Gordon, C.T., Kanae,
604 S., Kowalczyk, E., Lawrence, D., Liu, P., Lu, C-H., Malyshev, S., McAvaney, B., Mitchell, K.,
605 Mocko, D., Oki, T., Oleson, K., Pitman, A., Sud, Y.C., Taylor, C.M., Verseghy, D., Vasic, R.,
606 Xue, Y., & Yamada, T. (2004). Regions of strong coupling between soil moisture and
607 precipitation. *Science*, 305(5687), 1138–1140. <https://doi.org/10.1126/science.1100217>
- 608 Koster, R. D., Sud, Y. C. , Guo, Z., Dirmeyer, P. A., Bonan, G., Oleson, K. W., Chan, E.,
609 Verseghy, D., Cox, P., Davies, H., Kowalczyk, E., Gordon, C. T. , Kanae, S., Lawrence, D., Liu,
610 P., Mocko, D., Lu, C., Mitchell, K., Malyshev, S., McAvaney, B., Oki, T., Yamada, T., Pitman,
611 A., Taylor, C. M., Vasic, R., & Xue, Y. (2006). GLACE: The Global Land–Atmosphere
612 Coupling Experiment. Part I: Overview. *Journal of Hydrometeorology*, 7(4), 590-610.
613 <https://doi.org/10.1175/JHM510.1>
- 614 Kustas, W., & Anderson, M. (2009). Advances in thermal infrared remote sensing for land
615 surface modeling. *Agricultural and Forest Meteorology*, 149(12), 2071-2081.
616 <https://doi.org/10.1016/j.agrformet.2009.05.016>
- 617 Kustas, W. P., Nieto, H., Morillas, L., Anderson, M. C., Alfieri, J. G., Hipps, L. E.,
618 Villagarcia, L., Domingo, F., & Garcia, M. (2016). Revisiting the paper “Using radiometric
619 surface temperature for surface energy flux estimation in Mediterranean drylands from a two-
620 source perspective”. *Remote Sensing of Environment*, 184, 645-653.
621 <https://doi.org/10.1016/j.rse.2016.07.024>
- 622 Lawrence, D., Fisher, R., Koven, C., Oleson, K., Swenson, S., Vertenstein, M., Andre, B.,
623 Bonan, G., Ghimire, B., & van Kampenhout, L. (2018). Technical description of version 5.0 of
624 the Community Land Model (CLM), Natl. Cent. Atmospheric Res. (NCAR),
625 https://www.cesm.ucar.edu/models/cesm2/land/CLM50_Tech_Note.pdf 2018
- 626 Lawrence, D. M., Fisher, R. A., Koven, C. D., Oleson, K. W., Swenson, S. C., Bonan, G.,
627 Collier, N., Ghimire, B., van Kampenhout, L., Kennedy, D., Kluzek, E., Lawrence, P. J., Li, F.,
628 Li, H., Lombardozzi, D., Riley, W. J., Sacks, W. J., Shi, M., Vertenstein, M., Wieder, W. R., Xu,
629 C., Ali, A. A., Badger, A. M., Bisht, G., van den Broeke, M., Brunke, M. A., Burns, S. P., Buzan,
630 J., Clark, M., Craig, A., Dahlin, K., Drewniak, B., Fisher, J. B., Flanner, M., Fox, A. M.,
631 Gentine, P., Hoffman, F., Keppel-Aleks, G., Knox, R., Kumar, S., Lenaerts, J., Leung, L. R.,
632 Lipscomb, W. H., Lu, Y., Pandey, A., Pelletier, J. D., Perket, J., Randerson, J. T., Ricciuto, D.
633 M., Sanderson, B. M., Slater, A., Subin, Z. M., Tang, J., Thomas, R. Q., Val Martin, M., & Zeng,
634 X. (2019). The Community Land Model version 5: Description of new features, benchmarking,
635 and impact of forcing uncertainty. *Journal of Advances in Modeling Earth Systems*, 11, 4245–
636 4287. <https://doi.org/10.1029/2018MS001583>
- 637 Levine, P. A., Randerson, J. T., Swenson, S. C., & Lawrence, D. M. (2016). Evaluating the
638 strength of the land–atmosphere moisture feedback in Earth system models using satellite
639 observations. *Hydrology and Earth System Sciences*, 20(12), 4837-4856.
640 <https://doi.org/10.5194/hess-20-4837-2016>
- 641 Liao, W., Liu, X., Burakowski, E., Wang, D., Wang, L., & Li, D. (2020). Sensitivities and
642 responses of land surface temperature to deforestation-induced biophysical changes in two global
643 earth system models. *Journal of Climate*, 33(19), 8381-8399. <https://doi.org/10.1175/JCLI-D-19-0725.1>
- 644 Long, D., Longuevergne, L., & Scanlon, B. R. (2014). Uncertainty in evapotranspiration
645 from land surface modeling, remote sensing, and GRACE satellites. *Water Resources Research*,
646 50(2), 1131-1151. <https://doi.org/10.1002/2013WR014581>

- 648 Long, D., Yan, L., Bai, L., Zhang, C., Li, X., Lei, H., Yang, H., Tian, F., Zeng, C., Meng,
649 X. & Shi, C. (2020). Generation of MODIS-like land surface temperatures under all-weather
650 conditions based on a data fusion approach. *Remote Sensing of Environment*, 246, 111863.
651 <https://doi.org/10.1016/j.rse.2020.111863>
- 652 Ma, X., Jin, J., Zhu, L., & Liu, J. (2021). Evaluating and improving simulations of diurnal
653 variation in land surface temperature with the Community Land Model for the Tibetan Plateau.
654 *PeerJ*, 9, e11040. <https://doi.org/10.7717/peerj.11040>
- 655 Mallick, K., Toivonen, E., Trebs, I., Boegh, E., Cleverly, J., Eamus, D., Koivusalo, H.,
656 Drewry, D., Arndt, S.K., Griebel, A. & Beringer, J. (2018). Bridging Thermal Infrared Sensing
657 and Physically-Based Evapotranspiration Modeling: From Theoretical Implementation to
658 Validation Across an Aridity Gradient in Australian Ecosystems. *Water Resources Research*,
659 54(5), 3409-3435. <https://doi.org/10.1029/2017wr021357>
- 660 Mallick, K., Trebs, I., Boegh, E., Giustarini, L., Schlerf, M., Drewry, D.T., Hoffmann, L.,
661 Von Randow, C., Kruijt, B., Araùjo, A. & Saleska, S. (2016). Canopy-scale biophysical controls
662 of transpiration and evaporation in the Amazon Basin. *Hydrology and Earth System Sciences*,
663 20(10), 4237-4264. <https://doi.org/10.5194/hess-20-4237-2016>.
- 664 Mallick, K., Baldocchi, D., Jarvis, A., Hu, T., Trebs, I., Sulis, M., Bhattarai, N., Bossung,
665 C., Eid, Y., Cleverly, J. & Beringer, J. (2022). Insights Into the Aerodynamic Versus Radiometric
666 Surface Temperature Debate in Thermal-Based Evaporation Modeling. *Geophysical Research
667 Letters*, 49(15), e2021GL097568. <https://doi.org/10.1029/2021GL097568>
- 668 Massmann, A., Gentine, P., and Lin, C. (2019). When does vapor pressure deficit drive or
669 reduce evapotranspiration? *Journal of Advances in Modeling Earth Systems*, 11, 3305–3320.
670 <https://doi.org/10.1029/2019MS001790>
- 671 Medlyn, B.E., Duursma, R.A., Eamus, D., Ellsworth, D.S., Prentice, I.C., Barton, C.V.M.,
672 Crous, K.Y., De Angelis, P., Freeman, M., & Wingate, L. (2011). Reconciling the optimal and
673 empirical approaches to modelling stomatal conductance. *Global Change Biology*, 17: 2134–
674 2144. <https://doi.org/10.1111/j.1365-2486.2010.02375.x>
- 675 Mitchell, K.E., Lohmann, D., Houser, P.R., Wood, E.F., Schaake, J.C., Robock, A.,
676 Cosgrove, B.A., Sheffield, J., Duan, Q., Luo, L. and Higgins, R.W. (2004). The multi-institution
677 North American Land Data Assimilation System (NLDAS): Utilizing multiple GCIP products
678 and partners in a continental distributed hydrological modeling system. *Journal of Geophysical
679 Research: Atmospheres*, 109(D7). <https://doi.org/10.1029/2003JD003823>.
- 680 Meier, R., Davin, E. L., Bonan, G. B., Lawrence, D. M., Hu, X., Duveiller, G., Prigent, C.,
681 & Seneviratne, S. I. (2022). Impacts of a revised surface roughness parameterization in the
682 Community Land Model 5.1. *Geoscientific Model Development*, 15, 2365–2393,
683 <https://doi.org/10.5194/gmd-15-2365-2022>
- 684 Monteith, J. L. (1965). Evaporation and environment. In *Symposia of the society for
685 experimental biology* (Vol. 19, pp. 205-234). Cambridge University Press (CUP) Cambridge.
686 <https://repository.rothamsted.ac.uk/item/8v5v7/evaporation-and-environment>
- 687 Monteith, J. L. (1995). Accommodation between transpiring vegetation and the convective
688 boundary layer. *Journal of Hydrology*, 166(3-4), 251-263. [https://doi.org/10.1016/0022-1694\(94\)05086-D](https://doi.org/10.1016/0022-1694(94)05086-D)
- 690 Morrow, N., & Friedl, M.A. (1998). Modeling biophysical controls on land surface
691 temperature reflectance in grasslands. *Agricultural and Forest Meteorology*, 92(3), 147-161.
692 [https://doi.org/10.1016/S0168-1923\(98\)00098-7](https://doi.org/10.1016/S0168-1923(98)00098-7)

- 693 Mott, K. A. (2007). Leaf hydraulic conductivity and stomatal responses to humidity in
694 amphistomatous leaves. *Plant, Cell & Environment*, 30(11), 1444-1449.
695 <https://doi.org/10.1111/j.1365-3040.2007.01720.x>
- 696 Pastorello, G., Trotta, C., Canfora, E., Chu, H., Christianson, D., Cheah, Y.W., Poindexter,
697 C., Chen, J., Elbashandy, A., Humphrey, M. and Isaac, P. (2020), The FLUXNET2015 dataset
698 and the ONEFlux processing pipeline for eddy covariance data. *Scientific Data* 7, 225,
699 <https://doi.org/10.1038/s41597-020-534-3>
- 700 Penman, H. L. (1948). Natural evaporation from open water, bare soil and grass.
701 Proceedings of the Royal Society of London. Series A. *Mathematical and Physical Sciences*,
702 193(1032), 120-145. <https://doi.org/10.1098/rspa.1948.0037>
- 703 Reichstein, M., Tenhunen, J. D., Rouspard, O., Ourcival, J.-M., Rambal, S., Dore, S., &
704 Valentini, R. (2002). Ecosystem respiration in two Mediterranean evergreen Holm Oak forests:
705 drought effects and decomposition dynamics. *Functional Ecology*, 16, 27–
706 39, <https://doi.org/10.1046/j.0269-8463.2001.00597.x>
- 707 Sellers, P. J., Mintz, Y., Sud, Y. C., & Dalcher, A. (1986). A Simple Biosphere Model
708 (SIB) for Use within General Circulation Models. *Journal of Atmospheric Sciences*, 43(6), 505-
709 531. [https://doi.org/10.1175/1520-0469\(1986\)043<0505:ASBMFU>2.0.CO;2](https://doi.org/10.1175/1520-0469(1986)043<0505:ASBMFU>2.0.CO;2)
- 710 Siemann, A. L., Coccia, G., Pan, M., & Wood, E. F. (2016) Development and analysis of a
711 long term, global, terrestrial land surface temperature dataset based on HIRS satellite retrievals.
712 *Journal of Climate*, 29(10), 3589– 3606. <https://doi.org/10.1175/JCLI-D-15-0378.1>
- 713 Thakur, G., Schymanski, S. J., Mallick, K., Trebs, I., & Sulis, M. (2022). Downwelling
714 longwave radiation and sensible heat flux observations are critical for surface temperature and
715 emissivity estimation from flux tower data. *Scientific Reports*, 12(1), 8592.
716 <https://doi.org/10.1038/s41598-022-12304-3>
- 717 Tiktak, A., & Bouten, W. (1994), Soil water dynamics and long-term water balances of a
718 Douglas fir stand in the Netherlands. *Journal of Hydrology*, 156(1-4), 265-283.
719 [https://doi.org/10.1016/0022-1694\(94\)90081-7](https://doi.org/10.1016/0022-1694(94)90081-7)
- 720 Trebs, I., Mallick, K., Bhattarai, N., Sulis, M., Cleverly, J., Woodgate, W., Silberstein, R.,
721 Hinko-Najera, N., Beringer, J., Meyer, W.S. and Su, Z. (2021). The role of aerodynamic
722 resistance in thermal remote sensing-based evapotranspiration models. *Remote Sensing of*
723 *Environment*, 264, 112602. <https://doi.org/10.1016/j.rse.2021.112602>
- 724 Trigo, I. F., Boussetta, S., Viterbo, P., Balsamo, G., Beljaars, A., & Sandu, I. (2015).
725 Comparison of model land skin temperature with remotely sensed estimates and assessment of
726 surface-atmosphere coupling. *Journal of Geophysical Research: Atmospheres*. 120(23), 12,096–
727 12,111. <https://doi.org/10.1002/2015JD023812>
- 728 Ukkola, A. M., Haughton, N., De Kauwe, M. G., Abramowitz, G., & Pitman, A. J. (2017).
729 FluxnetLSM R package (v1.0): A community tool for processing FLUXNET data for use in land
730 surface modelling. *Geoscientific Model Development*, 10, 3379–3390,
731 <https://doi.org/10.5194/gmd-10-3379-2017>
- 732 Wang, A., M. Barlage, X. Zeng, & C. S. Draper (2014), Comparison of land skin
733 temperature from a land model, remote sensing and in situ measurement. *Journal of Geophysical*
734 *Research: Atmospheres*, 119, 3093–3106, <https://doi.org/10.1002/2013JD021026>.
- 735 Wang, S., Pan, M., Mu, Q., Shi, X., Mao, J., Brümmer, C., Jassal, R.S., Krishnan, P., Li, J.
736 and Black, T.A. (2015). Comparing evapotranspiration from Eddy covariance measurements,
737 water budgets, remote sensing, and land surface models over Canada. *Journal of*
738 *Hydrometeorology*, 16(4), 1540–1560. <https://doi.org/10.1175/Jhm-D-14-0189.1>

739 Yuan, X., Hamdi, R., Ochege, F. U., De Maeyer, P., Kurban, A., & Chen, X. (2021).
740 Assessment of surface roughness and fractional vegetation coverage in the CoLM for modeling
741 regional land surface temperature. *Agricultural and Forest Meteorology*, 303, 108390.
742 <https://doi.org/10.1016/j.agrformet.2021.108390>

743 Zeng, X., Wang, Z., & Wang, A. (2012). Surface skin temperature and the interplay
744 between sensible and ground heat fluxes over arid regions. *Journal of Hydrometeorology*, 13(4),
745 1359-1370. <https://doi.org/10.1175/JHM-D-11-0117.1>.

746 Zhang, B., Xia, Y., Long, B., Hobbins, M., Zhao, X., Hain, C., Li, Y., & Anderson, M.C.
747 (2020). Evaluation and comparison of multiple evapotranspiration data models over the
748 contiguous United States: Implications for the next phase of NLDAS (NLDAS-Testbed)
749 development. *Agricultural and Forest Meteorology*. 280, 107810.
750 <https://doi.org/10.1016/j.agrformet.2019.107810>

751 Zhang, X., Zhou, J., Liang, S., & Wang, D. (2021), A practical reanalysis data and thermal
752 infrared remote sensing data merging (RTM) method for reconstruction of a 1-km all-weather
753 land surface temperature. *Remote Sensing of Environment*, 260, 112437.
754 <https://doi.org/10.1016/j.rse.2021.112437>

755 Zheng, W., Wei, H., Wang, Z., Zeng, X., Meng, J., Ek, M., & Derber, J. (2012).
756 Improvement of daytime land surface skin temperature over arid regions in the NCEP GFS model
757 and its impact on satellite data assimilation, *Journal of Geophysical Research*, 117(D6), D06117,
758 <https://doi.org/10.1029/2011JD015901>

759
760
761
762
763
764